



Plasmonic gold–silver alloy on TiO₂ photocatalysts with tunable visible light activity



Sammy W. Verbruggen ^{a,b,*}, Maarten Keulemans ^a, Maria Filippoussi ^c, Delphine Flahaut ^d, Gustaaf Van Tendeloo ^c, Sylvie Lacombe ^d, Johan A. Martens ^b, Silvia Lenaerts ^{a,*}

^a Sustainable Energy and Air Purification, Department of Bioscience Engineering, University of Antwerp, Groenenborgerlaan 171, B-2020 Antwerp, Belgium

^b Center for Surface Chemistry and Catalysis, KU Leuven, Kasteelpark Arenberg 23, B-3001 Heverlee, Leuven, Belgium

^c EMAT, University of Antwerp, Groenenborgerlaan 171, B-2020 Antwerp, Belgium

^d IPREM UMR 5254, University of Pau et des Pays de l'Adour, F-64053 Pau 9, France

ARTICLE INFO

Article history:

Received 22 January 2014

Received in revised form 6 March 2014

Accepted 11 March 2014

Available online 21 March 2014

Keywords:

Photocatalysis

Surface plasmon resonance (SPR)

Titanium dioxide (TiO₂)

Stearic acid

Visible light

Gold

Silver

ABSTRACT

Adaptation of the photoresponse of anatase TiO₂ to match the solar spectrum is an important scientific challenge. Modification of TiO₂ with noble metal nanoparticles displaying surface plasmon resonance effects is one of the promising approaches. Surface plasmon resonance typically depends on chemical composition, size, shape and spatial organization of the metal nanoparticles in contact with TiO₂. Au_xAg_(1-x) alloy nanoparticles display strong composition-dependent surface plasmon resonance in the visible light region of the spectrum. In this work, a general strategy is presented to prepare plasmonic TiO₂-based photocatalysts with a visible light response that can be accurately tuned over a broad range of the spectrum. The application as self-cleaning material toward the degradation of stearic acid is demonstrated for a plasmonic TiO₂ photocatalyst displaying visible light photoactivity at the intensity maximum of solar light around 490 nm.

© 2014 Elsevier B.V. All rights reserved.

1. Introduction

TiO₂ based photocatalysis has been at the heart of UV light-driven chemical processes for several decades. Application fields of TiO₂ photocatalysis include artificial photosynthesis, water and air purification, sterilization and self-cleaning surfaces [1–7]. One of the major limitations remains the large band gap of the anatase TiO₂ semiconductor (ca. 3.2 eV), restricting the use of TiO₂ photocatalysis as a sustainable technology to applications governed by UV light. Adaptation of the photoresponse of anatase TiO₂ to match the solar spectrum is therefore an important scientific challenge. Exploiting surface plasmon resonance (SPR) effects through modification of TiO₂ with noble metal nanoparticles is one of the promising approaches [8,9].

Wavelength tuning of such an SPR system can be achieved by modifying the size, shape or type of the noble metals in contact with TiO₂, but the operating window of those strategies is limited to SPR shifts of several nm [10–13]. A promising alternative approach is offered by noble metal alloys. Colloidal Au–Ag alloy nanoparticles display highly tunable, composition- (and to lesser extent size-) dependent SPR maxima over a very broad range of visible light wavelengths (ca. 420–520 nm) [14–16]. Hence they make excellent candidates for shifting the photoresponse of TiO₂ from UV to visible light. Furthermore, the tailored synthesis of Au–Ag alloy nanoparticles and derived plasmonic photocatalysts as presented in this work, is easy to perform and does not require expensive equipment nor time-consuming techniques.

The wavelength range in which SPR occurs on these alloy nanoparticles, matches the range of high intensity wavelengths of solar light. This feature thus enables to design plasmonic photocatalysts tuned to a relevant range of the solar spectrum. This study shows how composition-dependent SPR of Au–Ag alloy nanoparticles can be used to prepare plasmonic TiO₂-based photocatalysts with SPR at specific, desired visible light wavelengths in a feasible, predictable and reliable way. Good overlap of the SPR absorption band and the intensity spectrum of incident light is an important

* Corresponding author. Tel.: +32 3 265 36 84; fax: +32 3 265 32 25.

** Corresponding author at: Sustainable Energy and Air Purification, Department of Bioscience Engineering, University of Antwerp, Groenenborgerlaan 171, B-2020 Antwerp, Belgium. Tel.: +32 3 265 36 84; fax: +32 3 265 32 25.

E-mail addresses: Sammy.Verbruggen@uantwerp.be (S.W. Verbruggen), Silvia.Lenaerts@uantwerp.be (S. Lenaerts).

design aspect for plasmonic enhancement [17]. Finally, using the proposed strategy visible light activity of plasmonic photocatalysts with their photoresponses tuned to the wavelength of maximum solar light intensity is demonstrated toward the photodegradation of a solid layer of stearic acid at ambient conditions under pure visible light (490 nm) illumination provided by LEDs.

2. Experimental

2.1. Plasmonic photocatalyst synthesis

Colloidal $\text{Au}_x\text{Ag}_{(1-x)}$ nanoparticles were prepared using a modified Turkevich procedure [18]. Appropriate amounts of 0.01 M $\text{HAuCl}_4 \cdot 3\text{H}_2\text{O}$ (Sigma–Aldrich, >99.9%) and 0.01 M AgNO_3 (Sigma–Aldrich, >99%) precursor solutions were diluted to avoid precipitation of AgCl and mixed, so that a total resulting metal concentration of 0.1 mM was obtained. The solution was stirred vigorously and brought to boil. 1 mL of a freshly prepared 1 wt% sodium citrate (Sigma–Aldrich, 99%) solution was quickly added to the boiling solution and left boiling for exactly 30 min.

For the preparation of the plasmonic catalysts a given amount of a commercially available TiO_2 source, P90 (Evonik, mean crystallite size 14 nm, specific surface area $90 \pm 20 \text{ m}^2 \text{ g}^{-1}$, 90% anatase, 10% rutile) was photo-impregnated [19] with a colloidal nanoparticle solution under vigorous stirring and UVA illumination (Philips Cleo UVA, 25 W, 365 nm) for 30 min. The resulting suspension was centrifugated, washed and dried overnight at 383 K. This procedure was repeated in order to obtain higher metal loadings.

2.2. Sample preparation and photocatalytic test

For the preparation of test samples, silicon wafers (15 mm × 30 mm) were cleaned ultrasonically in methanol and dried with compressed air. 50 μL of a 1 wt% suspension of catalyst powder in ethanol was drop casted on the wafer and dried at 363 K. A layer of stearic acid (SA) was applied by spin coating 100 μL of a 0.25 wt% solution of SA (Sigma–Aldrich, >98.5%) in chloroform at 1000 rpm for 1 min. The resulting sample was dried at 363 K. Before testing, the sample was allowed to equilibrate in the test environment for one hour [20].

The photocatalytic experiments involved illumination of the SA coated sample with a custom-made LED array consisting of eight LEDs, procured from Roithner LaserTechnic, emitting teal light ($\lambda_{\text{max}} = 490 \text{ nm}$, $\text{FWHM} = 30 \text{ nm}$, 26.8 mW cm^{-2} at sample distance). The test samples were located at a distance of 13 mm beneath the LED array. At regular time intervals, the remaining surface coverage of SA was measured using FTIR spectroscopy. The samples were placed at a fixed angle of 9° with the IR beam in order to minimize internal reflection effects. The SA concentration is related to the integrated absorbance in the wavenumber range 2800–3000 cm^{-1} , so that one unit of integrated area (in a.u. cm^{-1}) corresponds to 1.39×10^{16} SA molecules cm^{-2} , as determined by a calibration curve ($R^2 = 0.99$). This value is somewhat different from the corrected value of 9.7×10^{15} molecules cm^{-2} , reported by Mills et al. [21]. This is acceptable since the FTIR apparatus in this work is of a different type and, more importantly, by placing the wafers under a given angle the path length of the IR beam through the sample is changed. Given these circumstances and the good linear fit obtained in our calibration, we preferred sticking to the conversion factor as determined under the actual experimental conditions. The initial concentration in our experiments was typically around 8×10^{15} molecules cm^{-2} . The FTIR spectrophotometer was a Nicolet™ 380 (Thermo Fisher Scientific) equipped with ZnSe windows. All spectra were recorded in the wavenumber range

400–4000 cm^{-1} at a resolution of 2 cm^{-1} . For each measurement, eight spectra were averaged.

2.3. Characterization

Light intensity and photon fluxes were measured directly at sample distance with a calibrated Intensity spectrometer (Avantes Avaspec 3648) over the entire length of the LED array. Test samples were always located near the middle of the array, where the light intensity distribution is uniform.

UV–vis absorption spectra of colloidal $\text{Au}_x\text{Ag}_{(1-x)}$ nanoparticle solutions were measured with a Shimadzu UV–VIS 2501PC double beam spectrophotometer. UV–vis powder spectra were recorded with the same apparatus, equipped with a 60 mm BaSO_4 coated integrating sphere and a Photomultiplier R-446U detector.

Particle sizes of the colloidal nanoparticles were determined by dynamic light scattering (DLS) with a BIC 90 Plus apparatus (Brookhaven Instruments Corporation) equipped with a 659 nm laser (15 mW) at a 90° detection angle. Correlation functions were analyzed using the Igor Pro (v.6.02) software. The resulting decay time (τ) is converted into the hydrodynamic particle diameter using the Stokes–Einstein equation.

The elemental composition of the nanoparticles was verified by SEM–EDX (energy dispersive X-ray spectroscopy) using a JSM-5510 SEM operated at 30 kV equipped with an INCA 300 EDX microanalyzer. Samples adequate for TEM observations were prepared by drop casting a colloidal solution on holey, carbon-coated copper grids. STEM images and EDX maps were acquired by the EMAT group at UA using a Tecnai G2 electron microscope operated at 200 kV.

X-ray photoelectron spectra (XPS) were recorded using a Thermo Kα system with a hemispherical analyzer and a micro-focused (analysis area ca. $200 \mu\text{m}^2$) monochromatic radiation Al Kα line (1486.6 eV) operating at 75 W under a residual pressure of 1×10^{-7} mbar. The spectrometer pass energy was set to 200 eV for survey spectra and to 20 eV for core peak records. Surface charging was minimized using a neutralizer gun. All binding energies were referenced to the C1s peak at 285.0 eV. The treatment of core peaks was carried out using a nonlinear Shirley-type background [22]. A weighted least-squares fitting method using 70% Gaussian and 30% Lorentzian line shapes was applied to optimize the peak positions and areas. The quantification of surface composition was based on Scofield's relative sensitivity factors [23].

3. Results and discussion

3.1. Plasmonic photocatalyst synthesis and characterization

Suspensions of gold–silver alloy nanoparticles of various elemental compositions ($\text{Au}_x\text{Ag}_{(1-x)}$) were prepared using a modified Turkevich method as explained in Section 2.1. The chemical compositions of the alloys, verified using EDX, were in agreement with the nominal compositions (Table 1). The gold nanoparticles measured ca. 20 nm, while nanoparticles with 40% silver and more measured between 40 and 50 nm, according to dynamic light scattering data (Table 1). This can be accounted for by the fact that alloy nanoparticle formation begins with the formation of small gold nuclei and is then followed by growth through the incorporation of both gold and silver [24], implicating that a solution with more gold ions will give rise to many nuclei, and consequently many small particles while in a solution with more silver ions the few gold nuclei result in fewer but larger particles. For two samples, the nanoparticle size was also verified by TEM analysis of the plasmonic photocatalysts, i.e. after deposition of the colloidal nanoparticles on P90. Good agreement with the nanoparticle size

Table 1

Composition of the gold–silver alloy nanoparticles verified by EDX and particle sizes estimated by DLS and TEM.

Nominal composition [Au%–Ag%]	Measured composition (EDX) [Au%–Ag%]	Hydrodynamic diameter [nm] (DLS)	Diameter [nm] (TEM)
100–0	(98 ± 3)–(1 ± 2)	(19 ± 2)	(16 ± 2)
80–20	(78 ± 2)–(22 ± 2)	(24 ± 3)	–
60–40	(55 ± 5)–(45 ± 5)	(41 ± 5)	(40 ± 10)
40–60	(40 ± 1)–(60 ± 1)	(48 ± 5)	–
20–80	(25 ± 1)–(75 ± 1)	(43 ± 5)	–

as determined by DLS in solution was obtained, indicating that the particle size was not altered during the photodeposition process. N_2 adsorption–desorption measurements further indicated that the surface area of the TiO_2 powders was not influenced by modification with Au–Ag nanoparticles either.

Fig. 1a and b shows color pictures of the obtained colloidal nanoparticle solutions and plasmonic photocatalyst powders. The corresponding UV–vis absorbance spectra are presented in Fig. 1c and d. The appearance of one single SPR band in the spectrum of the nanoparticle suspensions depending on composition is in agreement with alloy formation. Other well-defined geometries such as core–shell nanoparticles would give rise to two SPR bands corresponding to the gold and silver phases, respectively [25,26]. The plasmonic photocatalysts display maximum SPR absorption in the visible light region between 470 and 540 nm (Fig. 1d), showing that visible light responsive catalysts can be created within a wavelength window of 70 nm by merely adapting the Au–Ag metal alloy composition. The higher refractive index of TiO_2 compared to water accounts for the red-shift of SPR maxima of the Au–Ag nanoparticles on the photocatalyst compared to the colloidal suspension (Fig. 1c vs. d) [27]. Scanning transmission electron microscopy (STEM) EDX mappings are displayed in Fig. 1e and f. The particles are well scattered across the TiO_2 surface, indicating no

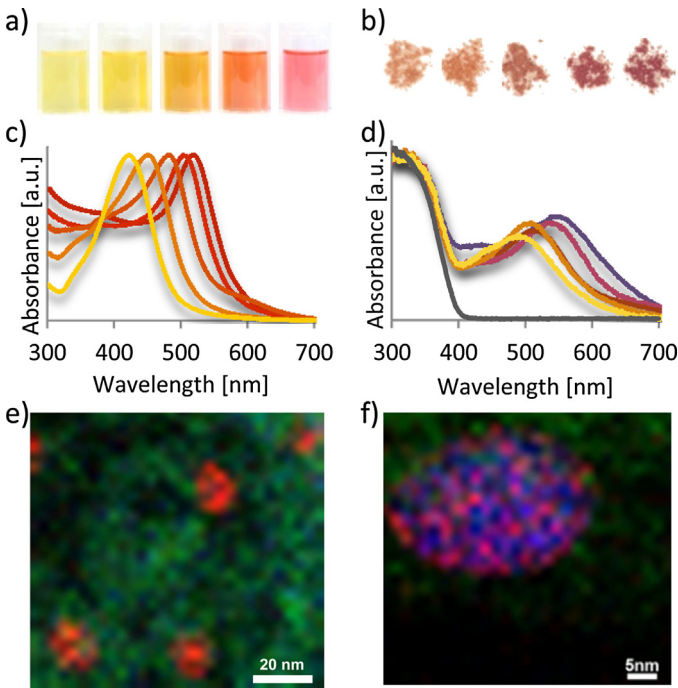


Fig. 1. Photographs of $Au_xAg_{(1-x)}$ with x from left to right 0.2, 0.4, 0.6, 0.8 and 1.0 of (a) colloidal alloy nanoparticle solutions and (b) plasmonic photocatalyst powders obtained after photodeposition of the colloidal nanoparticles on P90. Corresponding UV–vis absorption spectra of (c) colloidal $Au_xAg_{(1-x)}$ nanoparticle solutions and (d) plasmonic $Au_xAg_{(1-x)}$ –P90 photocatalysts (the gray curve corresponds to crude P90). STEM-EDX maps of (e) 100% gold nanoparticles on P90 (Au: red, Ti: green) and (f) and $Au_{0.6}Ag_{0.4}$ alloy nanoparticle on P90. (For interpretation of the references to color in this figure legend, the reader is referred to the web version of the article.)

clustering occurred during the deposition. Fig. 1f nicely shows a random distribution of gold and silver in the alloy nanoparticles.

The metallic nature of the alloy nanoparticles as well as the quantitative deposition on the TiO_2 substrate were confirmed by XPS. The results are presented in Table 2 and Fig. 2. The $Ti2p$, $O1s$, $Au4f$, $Ag3d$ and $C1s$ core peaks were recorded. The $Ti2p$ peaks are characteristic of Ti^{4+} in TiO_2 with two main components at 458.8 and 464.5 eV associated with $Ti2p_{3/2}$ and $Ti2p_{1/2}$ orbitals, and two satellites at 472 and 477 eV. The $O1s$ peaks exhibit two components: one at 530 eV attributed to oxygen of TiO_2 and another at 531.5 eV attributed to oxygen of surface hydroxyl groups. The $Ag3d$ core peaks are split into two components, $Ag3d_{5/2}$ and $Ag3d_{3/2}$, due to spin–orbit coupling ($\Delta BE(Ag3d_{5/2-3/2}) = 6$ eV). In the same manner, two components $Au4f_{7/2}$ and $Au4f_{5/2}$ are observed for the Au core peaks separated by 3.6 eV. The Au $4f_{7/2}$ core peaks located at 83.5–84.0 eV are assigned to metallic Au as the measured $Au4f$ core peaks occur at lower energies than expected for bulk metallic gold (84.0 eV), which could be explained by interaction with the TiO_2 substrate [26,28,29]. The binding energies of the $Ag3d_{5/2}$ core peaks are characteristic of metallic silver. Moreover, the $\Delta BE(Ag3d_{5/2}-Au4f_{7/2})$ is close to 284.2 eV for all the samples, confirming that the nature of the bond is irrespective of the nanoparticle composition. The quantitative analyses deduced from XPS allow an estimation of the total metal content, which is close to the nominal one (0.3 at%) within the error margin. No signal of $Au4f$ core peaks has been recorded for the sample with 20% Au, since the present gold content was below the detection limit (ca. 0.1 at%).

3.2. Visible light photocatalytic activity: self-cleaning surfaces

In our previous work is shown that SPR of $Au_xAg_{(1-x)}$ nanoparticles of a given size shows third-order dependence on the gold fraction, but can also be satisfactorily approached by a linear trend, especially when nanoparticles of different sizes are considered [16]. The present set of nanoparticles obeys such relationship of SPR wavelength and composition in suspension, as well as after deposition on TiO_2 (Fig. 3a and b). A similar trend between gold content and SPR wavelength has also been observed in the case of bimetallic Au–Ag nanoparticles on a ZnO substrate [30]. Consequently, this linear regression can be used as a calibration curve to predict which alloy composition is required for preparing a plasmonic photocatalyst with SPR at a specified wavelength. Based on the linear trend between SPR and composition (Fig. 3b), an alloy composition of 30% gold and 70% silver displays SPR at

Table 2

Binding energies of Au and Ag determined by XPS on 0.3 at% $Au_xAg_{(1-x)}$ nanoparticles on P90.

Composition [Au%–Ag%]	Au $4f_{7/2}$ [eV]	Ag $3d_{5/2}$ [eV]	Total metal loading [at%]
100–0	83.45	–	0.2 ± 0.1
80–20	83.78	367.92	0.2 ± 0.1
60–40	83.61	367.85	0.2 ± 0.1
40–60	84.00	368.36	0.3 ± 0.1
20–80	–	368.24	0.2 ± 0.1

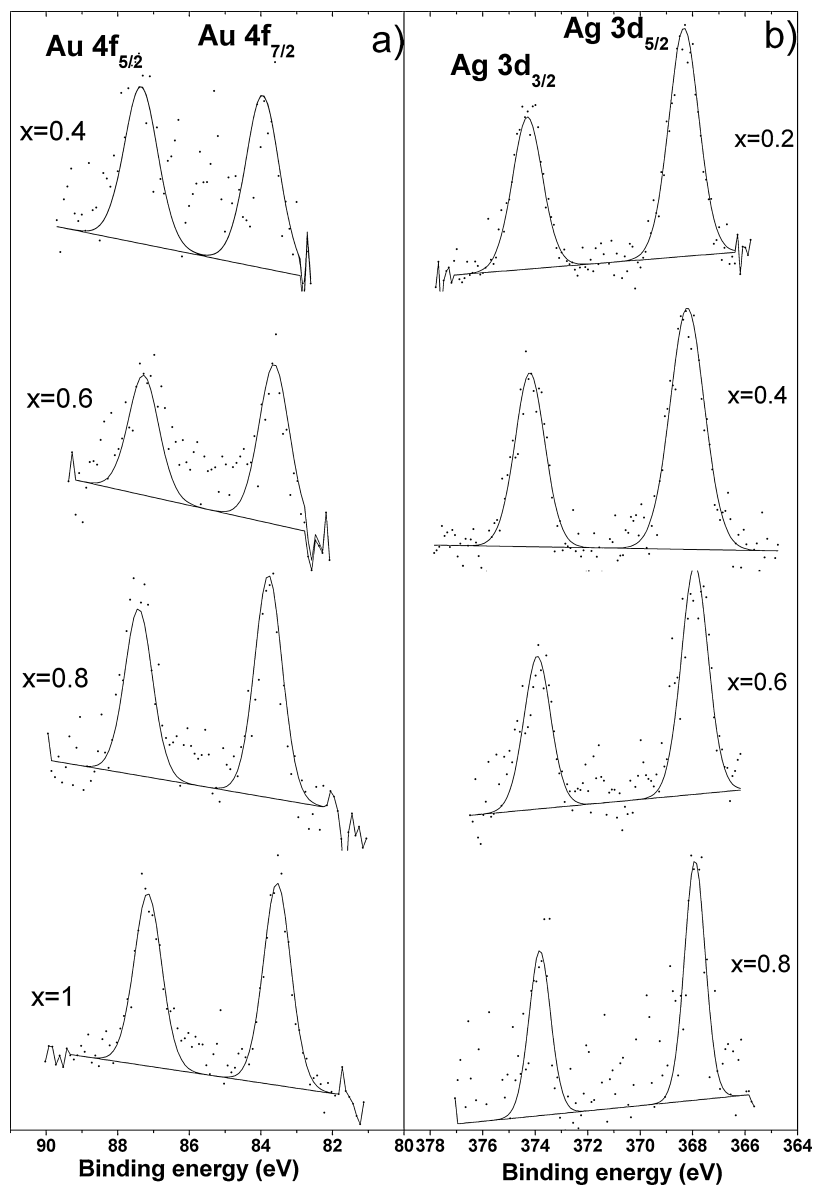


Fig. 2. XPS spectra for 0.3 at% $\text{Au}_x\text{Ag}_{(1-x)}$ nanoparticles on P90. (a) $\text{Au} 4f$ and (b) $\text{Ag} 3d$ XPS scans for different samples with varying alloy composition.

490 nm when deposited on TiO_2 , corresponding to the solar light intensity maximum. Therefore plasmonic catalysts were prepared using $\text{Au}_{0.3}\text{Ag}_{0.7}$ nanoparticles at loadings of 0.25, 0.5, 1.5 and 2.5 wt%. For comparative purposes, TiO_2 P90 was also loaded with

$\text{Au}_{0.55}\text{Ag}_{0.45}$ and pure Au nanoparticles that display SPR red-shifted by 25 and 50 nm, respectively. For all these samples, SPR occurred exactly at the predicted wavelength (Fig. 3c), demonstrating the success of the proposed synthesis strategy.

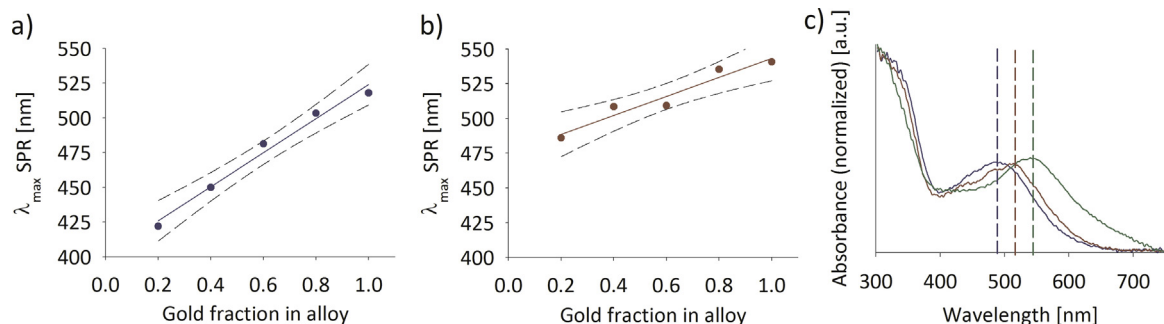


Fig. 3. (a) Plot of λ_{max} of the SPR band vs. the gold fraction x in the $\text{Au}_x\text{Ag}_{(1-x)}$ alloy nanoparticles in colloidal solution. The solid line represents a linear regression and the dotted curves the 95% confidence interval. (b) Same as in (a) in the case of nanoparticles deposited on TiO_2 P90. (c) UV-vis absorbance spectra of plasmonic photocatalysts containing 1.5 wt% of $\text{Au}_{0.3}\text{Ag}_{0.7}$ (blue), $\text{Au}_{0.55}\text{Ag}_{0.45}$ (red) and pure Au (green) nanoparticles on P90. λ_{max} corresponds to the expected SPR wavelength based on the regression in (b). (For interpretation of the references to color in this figure legend, the reader is referred to the web version of the article.)

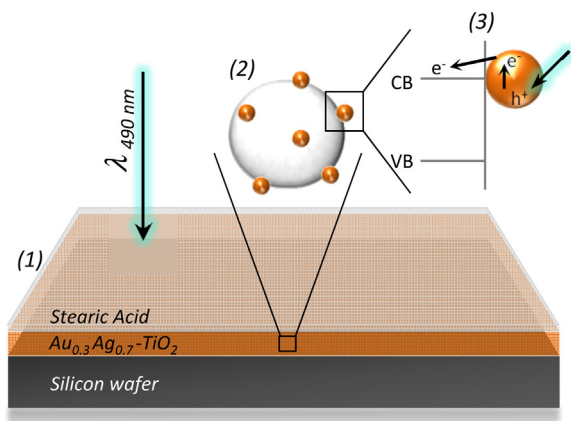


Fig. 4. (1) Schematic representation of the experimental set-up: a silicon wafer is coated with a layer of plasmonic photocatalyst and a solid layer of SA is applied by spin coating. Experiments are conducted under teal visible light (490 nm) provided by LEDs. (2) Schematic representation of a plasmonic photocatalyst particle: noble metal alloy nanoparticles deposited on TiO_2 P90. (3) Schematic illustration of the charge transfer mechanism at the metal nanoparticle- TiO_2 interface (see text).

The degradation of a thin, solid layer of stearic acid is a widely applied method for assessing the photocatalytic activity of self-cleaning materials [21,31,32]. SA is a good model compound for organic fouling on glass windows [33]. Mills and Wang have studied the photocatalytic mineralization reaction of SA by simultaneously monitoring the decrease in SA and the increase in CO_2 levels [21]. They have demonstrated that complete mineralization of SA to CO_2 can be achieved. The photocatalytic degradation can be monitored by following the integrated area of the FTIR absorbance bands in the range of 2800–3000 cm^{-1} , measured directly in transmission mode on the sample under study [34]. This range comprises the asymmetric $\nu_{\text{as}}(\text{CH}_3)$ vibration at 2958 cm^{-1} , asymmetric $\nu_{\text{as}}(\text{CH}_2)$ at 2923 cm^{-1} and symmetric $\nu_s(\text{CH}_2)$ at 2853 cm^{-1} of the SA hydrocarbon chain. For this test the plasmonic photocatalyst powders were deposited on a silicon wafer (8 $\mu\text{g cm}^{-2}$) and loaded with a layer of SA via spin coating (8×10^{15} SA molecules cm^{-2}). In the photocatalytic experiment (schematically illustrated in Fig. 4) a custom-made LED array served as light source, emitting teal light around 490 nm with a full width at half maximum (FWHM) of 30 nm. The intensity output was 26.8 mW cm^{-2} at a distance of 13 mm at the position of the samples, with a corresponding photon flux of 6.69×10^{16} photons $\text{cm}^{-2} \text{s}^{-1}$, measured with a calibrated intensity meter. The main advantages of this LED source are the peak emission wavelength close to the intensity maximum of sunlight and the narrow intensity distribution, ensuring that no contribution of UV light is present. The decrease of the SA concentration during illumination was monitored by means of the integrated FTIR absorbance in the range of 2800–3000 cm^{-1} as explained in Section 2 (Fig. 5a). Ollis explains how a zero order kinetic model adequately describes the rate of SA degradation on non-porous catalyst layers [35]. In our system, however, the presence of interparticle voids leads to an apparent positive reaction order (Fig. 5b). Therefore only the initial degradation rate, as derived from the first, linear part of the SA degradation curves, was considered in the further evaluation of the photocatalytic efficiency of the samples. The efficiency of the different samples is finally expressed as the formal quantum efficiency (FQE), recommended by IUPAC and corresponding to the rate of removal of SA molecules over the rate of incident photons.

FQE values obtained under 490 nm illumination are plotted in Fig. 6. In the absence of plasmonic nanoparticles (crude P90) there is no significant SA degradation. Application of $\text{Au}_{0.3}\text{Ag}_{0.7}$ nanoparticles significantly enhances the photocatalytic activity. Initially, the

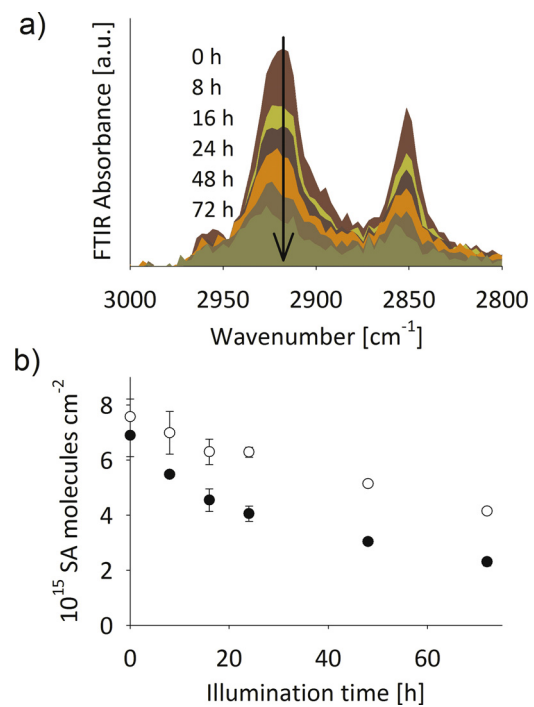


Fig. 5. (a) Evolution of the FTIR absorbance spectra of SA in the region 3000–2800 cm^{-1} during illumination (490 nm) for a sample containing 1.5 wt% $\text{Au}_{0.3}\text{Ag}_{0.7}$ nanoparticles on P90. (b) Decrease of the SA concentration as a function of illumination time (at 490 nm) for samples containing 1.5 wt% $\text{Au}_{0.3}\text{Ag}_{0.7}$ nanoparticles (●) and $\text{Au}_{0.55}\text{Ag}_{0.45}$ nanoparticles (○) on P90. The error bars were determined as the standard deviations on the values obtained by measuring the test sample in two different positions.

FQE increases linearly with nanoparticle loading, but starts to saturate around 1.5 wt%, which was thus considered to be a sufficient load. SA is degraded at a rate of 2.62×10^{10} molecules $\text{cm}^{-2} \text{s}^{-1}$, corresponding to a FQE of 0.39×10^{-6} molecules per photon under pure visible light (490 nm) illumination. This SA degradation rate is more than 50% higher compared to TiO_2 catalysts decorated with silver nanoparticles under filtered visible light illumination [36]. TiO_2 P90 catalyst loaded with compositionally optimized $\text{Au}_{0.3}\text{Ag}_{0.7}$ is about four times more active compared to sub-optimum $\text{Au}_{0.55}\text{Ag}_{0.45}$ having a 25 nm red-shifted SPR. Also, the FQE for P90 loaded with Au nanoparticles with SPR maximum at 540 nm is almost 2.5 times lower. The slightly higher FQE for pure Au nanoparticles compared to $\text{Au}_{0.55}\text{Ag}_{0.45}$ on P90 may be attributed to their smaller particle size (ca. 20 nm vs. 40 nm). For a constant metal loading on P90, many small metal nanoparticles are able to absorb more light than few larger particles, which may contribute to the higher FQE despite the less efficient overlap of the plasmon band and the incident light spectrum.

Three mutually non-exclusive mechanisms have been proposed for explaining SPR-mediated semiconductor photocatalysis [37]. The first mechanism involves direct charge transfer of an electron from an excited plasmon state on the metal to the semiconductor conduction band. The second mechanism is based on strong enhancement of the electromagnetic near-field in close proximity of the excited plasmonic nanoparticles. The third mechanism relies on increasing the optical path length of incident photons by light scattering on the metal nanoparticles. By elimination, direct charge transfer is tentatively proposed as the prevailing mechanism in the present situation (schematically illustrated in Fig. 4(3)). The enhanced near-field mechanism requires a good overlap of the SPR absorption band and the incident light spectrum, as well as an energy match between the semiconductor's band gap energy and the energy associated with SPR [17,38,39]. Considering this

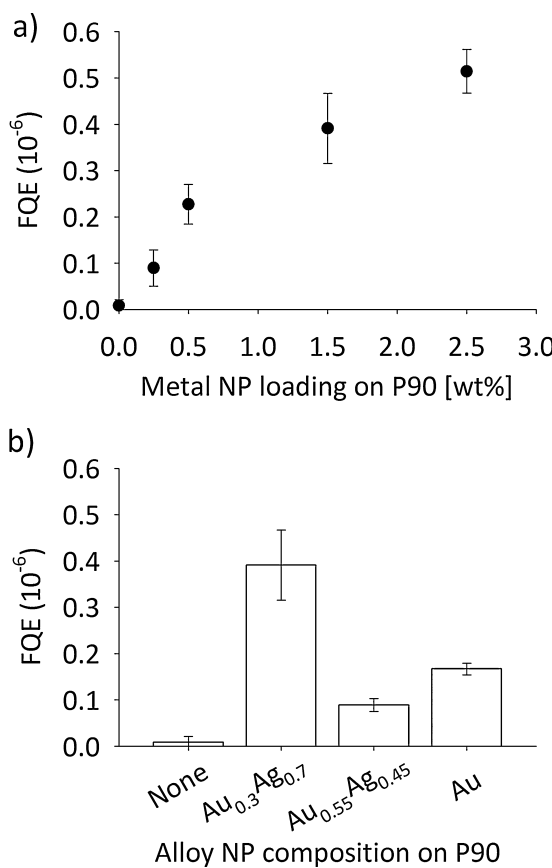


Fig. 6. (a) FQE under 490 nm illumination as a function of total metal loading of Au_{0.3}Ag_{0.7} nanoparticles on TiO₂ P90. (b) FQE under 490 nm illumination for catalysts with different alloy compositions. Except for the left bar (crude P90), the total metal loading was 1.5 wt%.

work, contribution of the near-field mechanism therefore seems less likely since the band gap of P90 (3.1 eV) is of much larger energy than those at which SPR occurs and hence the required overlap is poor. Also, the scattering mechanism seems rather unlikely as it mainly becomes important for nanoparticles with sizes approaching the incident light wavelength. Cases in which the plasmonic nanoparticles themselves directly act as the catalytic active site, as well as the light absorber in the absence of a semiconductor, have also been reported [40]. Therefore, elucidating the precise reaction mechanism remains challenging and is the subject of further research.

4. Conclusion

We have demonstrated a feasible, accurate strategy for boosting the visible light response of TiO₂ photocatalysts by tuning SPR of gold–silver alloy nanoparticles deposited on the surface. Colloidal suspensions of Au_xAg_(1-x) alloys with x between 0.2 and 1 show an intense SPR band in a broad visible light range from 420 to 520 nm. When deposited on TiO₂ P90, plasmonic photocatalysts can be prepared with SPR between 470 and 540 nm. As a case study, we have illustrated that, based on a linear trend between SPR and gold content, Au_{0.3}Ag_{0.7} nanoparticles on TiO₂ P90 specifically generate SPR at 490 nm, which matches the intensity maximum of the solar spectrum. This plasmonic photocatalyst proved to be significantly

more efficient toward stearic acid degradation under 490 nm illumination than pristine TiO₂ or other plasmonic photocatalysts with SPR deviating from the incident light wavelength. The ability to carefully control the light response of photoactive materials in a convenient way will assist the development of more efficient solar light driven photocatalytic processes.

Acknowledgements

S.W.V. acknowledges the Research Foundation of Flanders (FWO) for financial support. J.A.M. acknowledges the Flemish Government for long-term structural funding (Methusalem).

References

- [1] K. Kalyanasundaram, M. Graetzel, *Curr. Opin. Biotechnol.* 21 (2010) 298–310.
- [2] P.C. Maness, S. Smolinski, D.M. Blake, Z. Huang, E.J. Wolfrum, W.A. Jacoby, *Appl. Environ. Microbiol.* 65 (1999) 4094–4098.
- [3] I.P. Parkin, R.G. Palgrave, *J. Mater. Chem.* 15 (2005) 1689–1695.
- [4] S.W. Verbruggen, S. Ribbens, T. Tytgat, B. Hauchecorne, M. Smits, V. Meynen, P. Cool, J.A. Martens, S. Lenaerts, *Chem. Eng. J.* 174 (2011) 318–325.
- [5] S.W. Verbruggen, K. Masschaele, E. Moortgat, T.E. Korany, B. Hauchecorne, J.A. Martens, S. Lenaerts, *Catal. Sci. Technol.* 2 (2012) 2311–2318.
- [6] I.K. Konstantinou, T.A. Albanis, *Appl. Catal. B* 49 (2004) 1–14.
- [7] H.J. Zhang, G.H. Chen, D.W. Bahnemann, *J. Mater. Chem.* 19 (2009) 5089–5121.
- [8] X.M. Zhou, G. Liu, J.G. Yu, W.H. Fan, *J. Mater. Chem.* 22 (2012) 21337–21354.
- [9] A. Zielinska-Jurek, E. Kowalska, J.W. Sobczak, W. Lisowski, B. Ohtani, A. Zaleska, *Appl. Catal. B* 101 (2011) 504–514.
- [10] M. Grzelczak, J. Perez-Juste, P. Mulvaney, L.M. Liz-Marzan, *Chem. Soc. Rev.* 37 (2008) 1783–1791.
- [11] K.L. Kelly, E. Coronado, L.L. Zhao, G.C. Schatz, *J. Phys. Chem. B* 107 (2003) 668–677.
- [12] J. Kimling, M. Maier, B. Okenve, V. Kotaidis, H. Ballot, A. Plech, *J. Phys. Chem. B* 110 (2006) 15700–15707.
- [13] A. Sanchez-Iglesias, M. Grzelczak, J. Perez-Juste, L.M. Liz-Marzan, *Angew. Chem. Int. Ed.* 49 (2010) 9985–9989.
- [14] S. Link, Z.L. Wang, M.A. El-Sayed, *J. Phys. Chem. B* 103 (1999) 3529–3533.
- [15] L.M. Liz-Marzan, *Langmuir* 22 (2006) 32–41.
- [16] S.W. Verbruggen, M. Keulemans, J.A. Martens, S. Lenaerts, *J. Phys. Chem. C* 117 (2013) 19142–19145.
- [17] D.B. Ingram, P. Christopher, J.L. Bauer, S. Linic, *ACS Catal.* 1 (2011) 1441–1447.
- [18] J. Turkevich, P.C. Stevenson, J. Hillier, *Discuss. Faraday Soc.* 11 (1951) 55–75.
- [19] A. Tanaka, A. Ogin, M. Iwaki, K. Hashimoto, A. Ohnuma, F. Amano, B. Ohtani, H. Kominami, *Langmuir* 28 (2012) 13105–13111.
- [20] S. Deng, S.W. Verbruggen, S. Lenaerts, J.A. Martens, S. Van den Berghe, K. Devloo-Casier, W. Devulder, J. Dendooven, D. Deduytsche, C. Detavernier, *J. Vac. Sci. Technol. A* 32 (2014) 01A123, <http://dx.doi.org/10.1116/1.4847976>.
- [21] A. Mills, J.S. Wang, *J. Photochem. Photobiol. A* 182 (2006) 181–186.
- [22] D.A. Shirley, *Phys. Rev. B* 5 (1972) 4709–4714.
- [23] J.H. Scofield, *J. Electron. Spectrosc. Relat. Phenom.* 8 (1976) 129–137.
- [24] B. Rodriguez-Gonzalez, A. Sanchez-Iglesias, M. Giersig, L.M. Liz-Marzan, *Faraday Discuss.* 125 (2004) 133–144.
- [25] P. Mulvaney, *Langmuir* 12 (1996) 788–800.
- [26] A.Q. Wang, J.H. Liu, S.D. Lin, T.S. Lin, C.Y. Mou, *J. Catal.* 233 (2005) 186–197.
- [27] P. Christopher, H.L. Xin, S. Linic, *Nat. Chem.* 3 (2011) 467–472.
- [28] S. Arrii, F. Morfin, A.J. Renouprez, J.L. Rousset, *J. Am. Chem. Soc.* 126 (2004) 1199–1205.
- [29] R. Radnik, C. Mohr, P. Claus, *Phys. Chem. Chem. Phys.* 5 (2003) 172–177.
- [30] Y. Li, B. Zhang, J. Zhao, *J. Alloys Compd.* 586 (2014) 663–668.
- [31] Y. Paz, Z. Luo, L. Rabenberg, A. Heller, *J. Mater. Res.* 10 (1995) 2842–2848.
- [32] M.N. Ghazzal, N. Barthen, N. Chaoui, *Appl. Catal. B* 103 (2011) 85–90.
- [33] A. Mills, A. Lepre, N. Elliott, S. Bhopal, I.P. Parkin, S.A. O'Neill, *J. Photochem. Photobiol. A* 160 (2003) 213–224.
- [34] E. Allain, S. Besson, C. Durand, M. Moreau, T. Gacoin, J.P. Boilot, *Adv. Funct. Mater.* 17 (2007) 549–554.
- [35] D. Ollis, *Appl. Catal. B* 99 (2010) 478–484.
- [36] C.W. Dunnill, K. Page, Z.A. Aiken, S. Noimark, G. Hyett, A. Kafizas, J. Pratten, M. Wilson, I.P. Parkin, *J. Photochem. Photobiol. A* 220 (2011) 113–123.
- [37] S. Linic, P. Christopher, D.B. Ingram, *Nat. Mater.* 10 (2011) 911–921.
- [38] Z.W. Liu, W.B. Hou, P. Pavaskar, M. Aykol, S.B. Cronin, *Nano Lett.* 11 (2011) 1111–1116.
- [39] M.K. Kumar, S. Krishnamoorthy, L.K. Tan, S.Y. Chiam, S. Tripathy, H. Gao, *ACS Catal.* 1 (2011) 300–308.
- [40] M.J. Kale, T. Avanesian, P. Christopher, *ACS Catal.* 4 (2014) 116–128.